TISSUE ENGINEERING: Part A
Volume 26, Numbers 3 and 4, 2020

DOI: 10.1089/ten.tea.2019.0166

termis
Tissue Engineering
& Regenerative Medicine
International Society

ORIGINAL ARTICLE

3D-Printed Ceramic-Demineralized Bone Matrix Hyperelastic Bone Composite Scaffolds for Spinal Fusion

J. Adam Driscoll, MD,[1,2,*] Ryan Lubbe, MD,[1,2,*] Adam E. Jakus, PhD,[2–4] Kevin Chang, BS,[1,2] Meraaj Haleem, BA,[1,2] Chawon Yun, PhD,[1,2] Gurmit Singh, BS,[1,2] Andrew D. Schneider, MD,[1,2] Karina M. Katchko, MD,[1,2] Carmen Soriano, PhD,[5] Michael Newton, MS,[6] Tristan Maerz, PhD,[6,7] Xin Li, PhD, MD,[2] Kevin Baker, PhD,[6,8] Wellington K. Hsu, MD,[1,2] Ramille N. Shah, PhD,[2–4,6,9] Stuart R. Stock, PhD,[2,10] and Erin L. Hsu, PhD[1,2]

Although numerous spinal biologics are commercially available, a cost-effective and safe bone graft substitute material for spine fusion has yet to be proven. In this study, ''3D-Paints'' containing varying volumetric ratios of hydroxyapatite (HA) and human demineralized bone matrix (DBM) in a poly(lactide-co-glycolide) elastomer were three-dimensional (3D) printed into scaffolds to promote osteointegration in rats, with an end goal of spine fusion without the need for recombinant growth factor. Spine fusion was evaluated by manual palpation, and osteointegration and *de novo* bone formation within scaffold struts were evaluated by laboratory and synchrotron microcomputed tomography and histology. The 3:1 HA:DBM composite achieved the highest mean fusion score and fusion rate (92%), which was significantly greater than the 3D printed DBM-only scaffold (42%). New bone was identified extending from the host transverse processes into the scaffold macropores, and osteointegration scores correlated with successful fusion. Strikingly, the combination of HA and DBM resulted in the growth of bone-like spicules within the DBM particles *inside* scaffold struts. These spicules were not observed in DBM-only scaffolds, suggesting that *de novo* spicule formation requires both HA and DBM. Collectively, our work suggests that this recombinant growth factor-free composite shows promise to overcome the limitations of currently used bone graft substitutes for spine fusion.

Keywords: demineralized bone matrix, hydroxyapatite, 3D printing, osteointegration, spine fusion

Impact Statement

Currently, there exists a no safe, yet highly effective, bone graft substitute that is well accepted for use in spine fusion procedures. With this work, we show that a three-dimensional printed scaffold containing osteoconductive hydroxyapatite and osteoinductive demineralized bone matrix that promotes new bone spicule formation, osteointegration, and successful fusion (stabilization) when implemented in a preclinical model of spine fusion. Our study suggests that this material shows promise as a recombinant growth factor-free bone graft substitute that could safely promote high rates of successful fusion and improve patient care.

[1]Department of Orthopaedic Surgery, Northwestern University, Chicago, Illinois.
[2]Simpson Querrey Institute, Chicago, Illinois.
[3]Department of Materials Science and Engineering, Northwestern University Evanston, Illinois.
[4]Transplant Division, Department of Surgery, Northwestern University, Chicago, Illinois.
[5]Argonne National Laboratory, Argonne, Illinois.
[6]Orthopaedic Research Laboratory, Beaumont Health, Royal Oak, Michigan.
[7]Department of Orthopaedic Surgery, University of Michigan, Ann Arbor, Michigan.
[8]Department of Orthopaedic Surgery, Oakland University—William Beaumont School of Medicine, Rochester, Michigan.
Departments of [9]Biomedical Engineering and [10]Cell and Molecular Biology, Northwestern University, Evanston, Illinois.
Investigation performed at the Simpson Querrey Institute, Northwestern University, Chicago, Illinois.
*These authors contributed equally to this work.

Introduction

Spine fusion is among the most common orthopedic procedures and addresses disorders, including degenerative disc disease, disc herniation, segmental instability, trauma, and deformities of the spine. From 1998 to 2008, the number of spine fusions performed annually in the United States has more than doubled,[1] and it continues to rise. Pseudarthrosis (surgical nonunion) occurs in >10% of patients[2] and leads to poor patient-reported outcomes, the need for revision procedures, and increased cost of care.[3–5]

Successful bone regeneration and spine fusion requires a substrate that is both osteoinductive and osteoconductive. Osteoinductive materials promote recruitment of immature cells and stimulate those cells down the osteoblastic lineage, whereas osteoconductive substances provide a scaffold onto which newly formed bone can readily grow. While ceramics such as hydroxyapatite (HA) lack inherent osteoinductivity, are brittle, and handle poorly,[6] demineralized bone matrix (DBM)[7–9] is insufficient to yield high fusion rates when used without autogenous bone graft.[6] When used alone clinically, neither of these materials are an adequate substitute for autogenous bone graft for spine fusion. Conversely, recombinant human bone morphogenetic protein-2 (rhBMP-2) is an FDA-approved bone graft substitute for spine fusion that elicits high rates of fusion without autograft bone or bone graft extenders; however, serious complications associated with supraphysiologic dosing have drastically decreased its clinical use.[10–12] Thus, the lack of a universally accepted, safe bone graft substitute that promotes high rates of fusion remains a major clinical challenge.

Additive manufacturing techniques have recently been used in many disciplines of orthopedic surgery, including biomodels, surgical guides, and instrumentation. Three-dimensional (3D) printing, as one example, provides a wealth of options to customize the shape, stability, and biomechanical properties of surgical implants. Furthermore, recent developments now allow greater flexibility in ink composition to further enhance bone healing. Our prior work demonstrated that a 3D printable HA-based material, Hyperelastic Bone® (HB), showed promise as a bone graft extender with rhBMP-2 in a preclinical spine fusion model.[13] However, when used alone, the HB did not approach the ~100% fusion rate required of a bone graft substitute[13] to be tested clinically.

In this study, we investigate a recombinant growth factor-free material for improving osteointegration and spine fusion outcomes. This compositional variant of HB incorporates allograft-derived DBM particles into the HB ink. As an alternative to incorporating recombinant growth factor, we sought to improve preclinical outcomes by exploiting the potential synergistic effect of osteoconductive HA and osteoinductive DBM particles within composite scaffolds produced by 3D printing,[13–15] and we evaluated scaffold performance in the rat spine fusion model. We hypothesized that our novel additive manufacturing approach—which allows for the incorporation of human DBM particles within a surgically friendly ceramic material—would lead to osteointegration and spine fusion without the need for recombinant growth factor or autogenous bone harvest.

Materials and Methods

Ink synthesis and scaffold fabrication

Inks for 3D printing were synthesized as described previously[13] and consisted of five distinct combinations of polylactide-co-glycolide copolymer (PLG; 82:18 glycolide: lactide; Evonik Cyro), synthetic HA (Sigma-Aldrich; 1–30 μm particles) and/or DBM powder (Xtant Medical; 100–1000 μm particles milled and sieved to final diameter <80 μm). The relative amount of PLG was constant at 30 vol.%, and the 3D paints contained particle loadings of 70 vol.% HA (1:0 HA:DBM), 70 vol.% combined HA+DBM (3:1, 1:1, or 1:3 HA:DBM), or 70 vol.% DBM (0:1 HA:DBM), Table 1. A 3D-Bioplotter (EnvisionTEC, GmbH, Germany) was used to print the scaffolds via room-temperature syringe extrusion (410 μm diameter nozzle). Struts were printed with each progressive layer oriented 90° relative to the underlying layer, with a strut-to-strut spacing (''macropore size'') of 500 μm. After printing, the scaffolds were washed in 70% ethanol followed by sterile phosphate-buffered saline. The scaffolds were cut to size (15 × 4 × 3 mm) before implantation.

Cell culture and imaging

Rat bone marrow stromal cells were purchased from Lonza (Walkersville, MD). Low-passage cells were grown in basal media (mesenchymal stem cell basal medium and proliferation kit; Lonza) according to the manufacturer's instructions. Trypsinized cells were resuspended in Dulbecco's modified Eagle's medium containing 10% fetal bovine serum, Hepes buffer, L-glutamine, and antibiotic-antimycotic (Invitrogen). Cells were then inoculated onto cylindrical plugs cut from scaffolds printed with a 90° offset advancing angle using a 400 μm nozzle, with 500 μm strut-to-strut spacing (macropores). Cells/scaffolds were incubated at 37°C in 5% CO_2 until the indicated time points. For confocal imaging, cells/scaffolds were stained with calcein AM (green)/ethidium homodimer-1 (red) to visualize live and dead cells, respectively.

Table 1. Scaffold Composition and Animal Treatment Groups

Scaffold/Tx group	*Scaffold particle content (ratio HA:DBM)*	*HA particle content (vol.%)*	*DBM particle content (vol.%)*	*PLG (vol.%)*	N/*group*
HA-only	1:0	70	0	30	12
3:1 HA:DBM	3:1	52.5	17.5	30	12
1:1 HA:DBM	1:1	35	35	30	12
1:3 HA:DBM	1:3	17.5	52.5	30	12
DBM-only	0:1	0	70	30	12

DBM, demineralized bone matrix; HA, hydroxyapatite; PLG, polylactide-co-glycolide.

In vivo *study design*

Northwestern University's Institutional Animal Care and Use Committee approved the study, which was in compliance with the NIH Guide for Care and Use of Laboratory Animals. Sixty female Sprague–Dawley rats, aged 12–16 weeks, were randomly assigned to one of five treatment groups ($N = 12$/group). Rats received scaffolds composed of HA-only; 3:1, 1:1, or 1:3 HA:DBM; or DBM-only (Table 1).

Surgical procedure

Rats were anesthetized with inhalational isoflurane and monitored throughout the procedure. Posterolateral spine fusion (PLF) was performed as previously described.[16–19] A posterior midline incision was made over the lumbar spinous processes, followed by two separate fascial incisions 4 mm from the midline. The L4 and L5 transverse processes (TPs) were exposed via blunt dissection to create space for graft implantation, and the surgical site was irrigated with gentamicin solution. A high-speed burr was then used to decorticate the posterior L4–L5 TP surfaces, and grafts were placed bilaterally to bridge the L4–L5 intertransverse space (Fig. 1B). Fascial incisions were closed with monocryl sutures and skin incisions with wound clips. Buprenex and meloxicam were administered for 3 days postoperatively. Animals were allowed to eat, drink, and bear weight *ad libitum*.

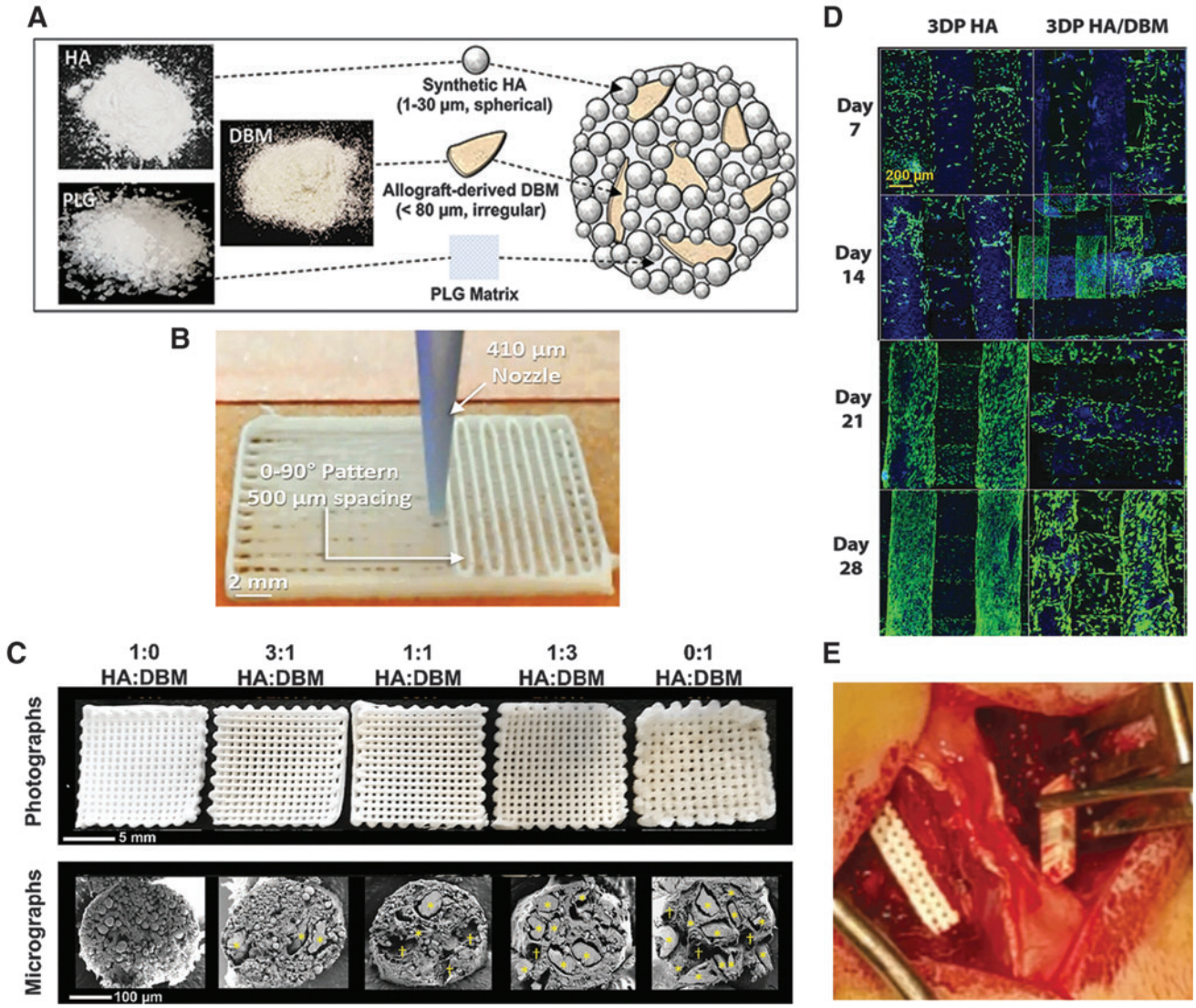

FIG. 1. Scaffold design and implantation. **(A, B)** Scaffold design and fabrication. **(C)** Images of unimplanted scaffolds. *Upper*: basic geometry of the scaffolds, with 90° aligned struts and visible channels (macropores) extending through the scaffolds. *Lower*: cross-sections of individual struts as imaged using scanning electron microscopy (plasma-coating with ~15 nm osmium metal, imaged with 3 kV accelerating voltage using a LEO Gemini 1525 at the EPIC facility, NUANCE Center, Northwestern University). The relative particle content [% HA (*upper*) vs. DBM (*lower*)] within the scaffolds is shown. Total particle content was held constant at 70% of the scaffold volume; the remaining 30% is PLG binder. *Yellow stars* identify DBM particles. **(D)** Laser-scanning confocal z-projections of 3D-stacks from live-dead stained scaffold seeded with primary rat bone marrow stromal cells. *Blue* is autofluorescence from the scaffold materials. **(E)** Intraoperative implantation of a scaffold. 3D, three-dimensional; DBM, demineralized bone matrix; HA, hydroxyapatite; SEM, scanning electron microscopy.

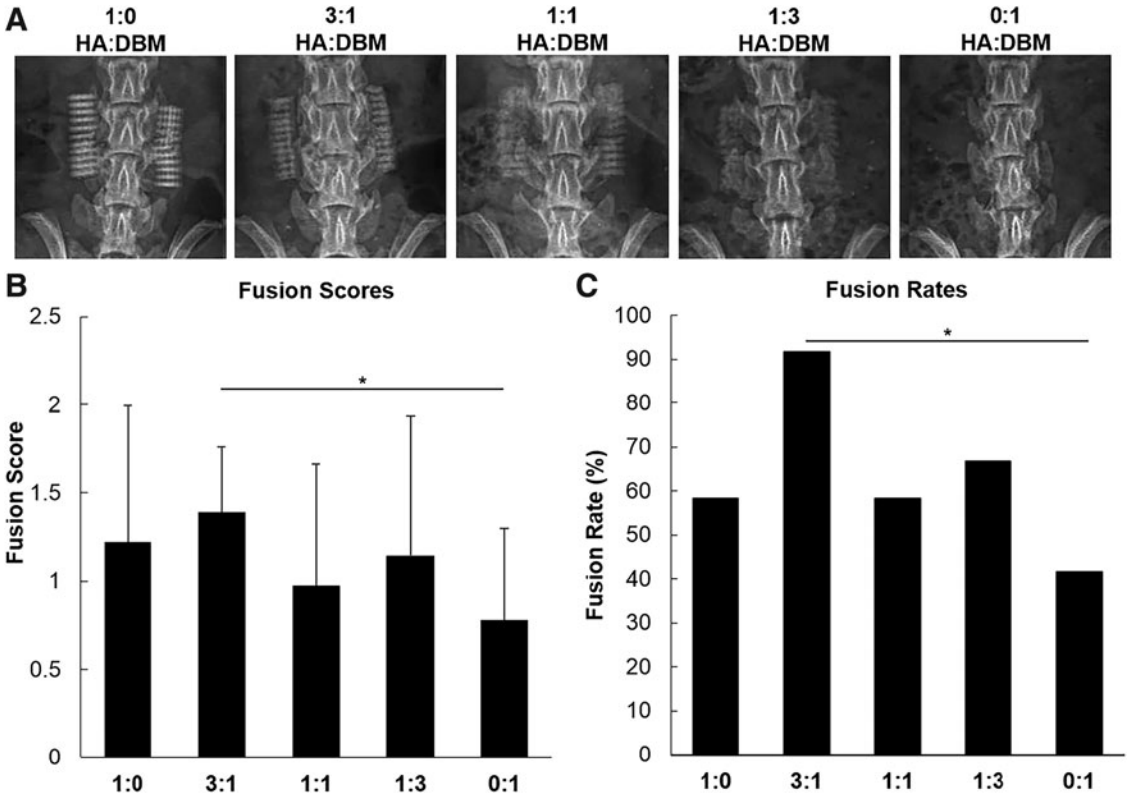

FIG. 2. Assessment of fusion. **(A)** Representative 8-week postoperative radiographs from each treatment group. Ratios represent relative HA:DBM particle content. **(B)** Fusion scores as determined by manual palpation by three blinded observers. Scoring was based on detectable motion between L4 and L5 segments. **(C)** Fusion rates were calculated based on fusion scores, where unilateral lack of motion was considered successfully fused.

Radiography and fusion scoring

Plain anteroposterior radiographs were taken 10 days postoperatively (following removal of wound clips) and before euthanasia at 8 weeks. Lumbar spines were harvested *en bloc*, fixed in 10% neutral-buffered formalin, and stored in 70% ethanol. All spines were then scored for fusion via manual palpation by three independent, blinded observers using an established scoring system for this model: ''0'' indicates detectable motion between segments bilaterally, ''1'' no motion between segments unilaterally and ''2'' no motion between segments bilaterally.[13,20–26] An average fusion score of ≥1 was considered a successfully fused spine.[17–19]

Microcomputed tomography and osteointegration scoring

Six spines per treatment group were imaged with laboratory microcomputed tomography (Laboratory microCT; VivaCT 80; Scanco Medical). Reconstruction was with an isotropic volume element (voxel) size of 17.5 μm. Three measures quantified the extent of fusion. The first was total bone volume (L4 and L5 TPs) on each side of the spine: contours were drawn around the bone within each slice using Amira software (Thermo Fisher Scientific), and segmentation was performed within the contours. The second measure of scaffold–bone interaction was based on the extent to which bone ''fingers'' penetrated into the scaffold, that is, osteointegration scoring system of 0 (minimum) to 3 (maximum) penetration, applied separately to each implant (Fig. 4A). The total osteointegration score for a scaffold summed scores for the medial surface (''medial endcap'' adjacent to the vertebral body), the scaffold body, and the lateral surface end (the ''lateral endcap'') for each TP. The third measure applied to spines with DBM scaffolds which were invisible in microCT: the peak-to-peak distance between adjacent bone fingers from the surface of the TP was defined as the bone ingrowth periodicity, and this was compared to the mid macropore-to-macropore distance in an unimplanted DBM scaffold. Bone integration into the scaffold body and around the sides of the scaffold (endcaps) provides resistance to different loading regimes: the former to flexion/extension and axial loading, and the latter to axial torsion as well. Incorporating all three scores into the total emphasizes the importance of both contact sites in restricting motion of the adjacent vertebrae.

The three spines per treatment group with highest fusion scores were imaged with synchrotron microCT with 2.35 μm

Table 2. Fusion Scores and Rates

Treatment group	N	*No. fused*	*Fusion rate (%)*	*Mean fusion score*
HA-only	12	7	58	1.2 ± 0.37
3:1 HA:DBM	12	11	92	1.4 ± 0.69
1:1 HA:DBM	12	7	58	1.0 ± 0.69
1:3 HA:DBM	12	8	67	1.1 ± 0.80
DBM-only	12	5	42	0.78 ± 0.52

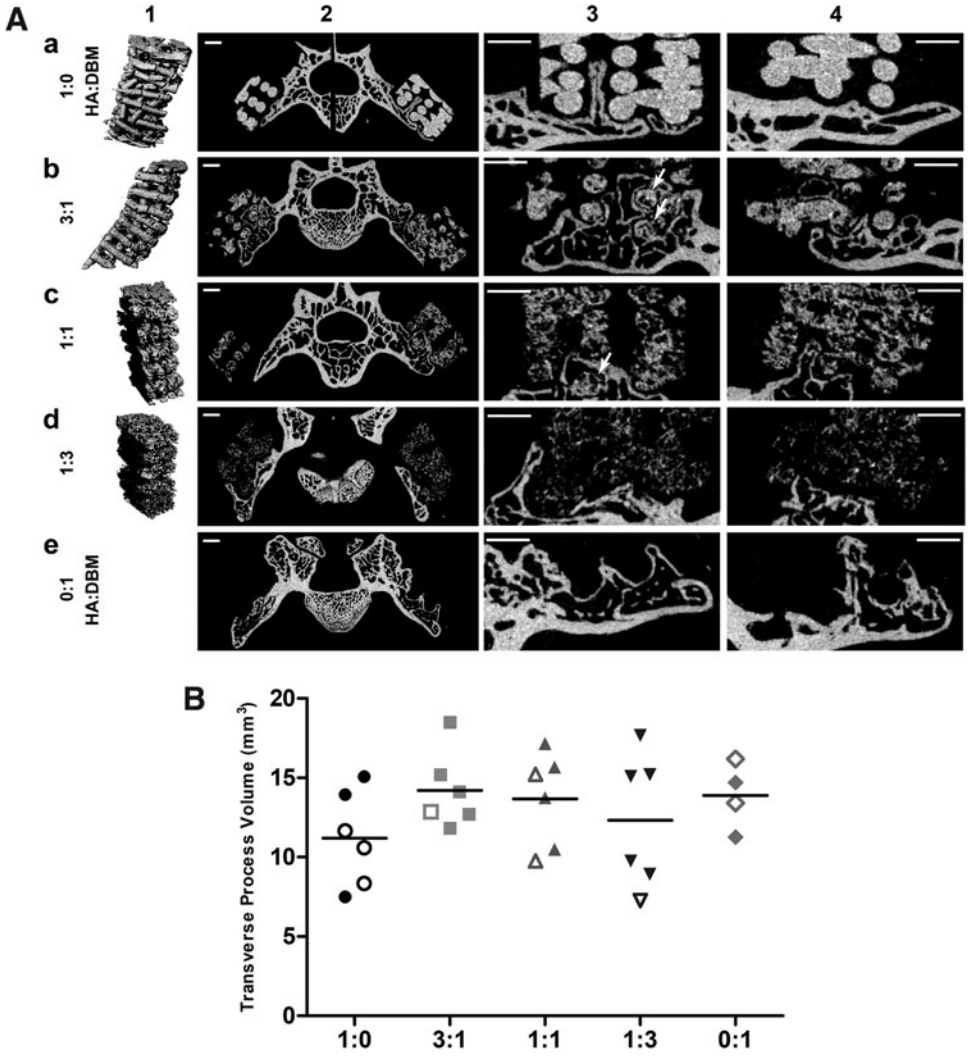

FIG. 3. Laboratory microCT. **(A)** Laboratory microCT images 8 weeks postoperative. Each row (*a–e*) corresponds to a different scaffold type. *Column 1* shows 3D renderings of the respective scaffolds, *column 2* shows slices covering the entire spine, *column 3* shows an enlarged area around one of the transverse processes from *column 2*, and *column 4* shows an enlargement of a different slice. The lighter the pixel in *columns 2–4*, the more heavily attenuating the corresponding voxel. *Column 3* symbols are identified in the text. Scale bars = 1 mm. **(B)** Laboratory microCT measurement of the volume of bilateral L4 and L5 transverse processes, which includes new bone growth into the scaffolds. Closed symbols denote spines scored as fused and open symbols unfused spines. microCT, microcomputed tomography.

isotropic voxels at beamline 2-BM, the Advanced Photon Source (APS), Argonne National Laboratory. The higher spatial resolution and contrast sensitivity was used to reveal details invisible in the laboratory microCT images. Spines were bisected longitudinally to fit the field of view, and the right half of each spine (entire scaffold and surrounding bone) was imaged. Unimplanted pieces of all five scaffold materials were also imaged.

Histology

Representative fused spines from each treatment group underwent histological analysis for visualization of evidence for endochondral bone formation.[16,18] Tissue processing was performed by the Northwestern Mouse Histology and Phenotyping Laboratory core facility, where spines were placed in Immunocal 12% formic acid solution (StatLab) for 72 h and processed using an ASP300S automated tissue processor (Leica Biosystems) for tissue dehydration, clearing, and paraffin infiltration. Specimens were then embedded in paraffin in a sagittal orientation and sectioned onto glass slides at a thickness of 5 μm. Staining was performed using Gill modified hematoxylin (Millipore), alcian blue, orange G, and eosin Y solution (Sigma-Aldrich). Masson's trichrome staining was performed using a Trichrome Stain Kit (Sigma-Aldrich).

Statistics

Statistics were performed using SPSS. Continuous variables were compared using one-way ANOVA for normally distributed data. Tukey's test was used for *post hoc* analyses. Fisher's exact test was used to compare the categorical data. Simple linear regression analysis was used to study the relationship between osteointegration and fusion scores. A p-value <0.05 was considered statistically significant.

Results

Cytocompatibility

In previous work, we showed that the 3D printed HA-only scaffold is biocompatible and supports osteogenic differentiation.[13] To confirm the biocompatibility of the DBM-containing scaffolds utilized in the current study, primary rat bone marrow stromal cells were seeded on 3D printed HA or HA-DBM scaffolds and incubated in growth media for up to 28 days. Confocal imaging showed that live cells (green)

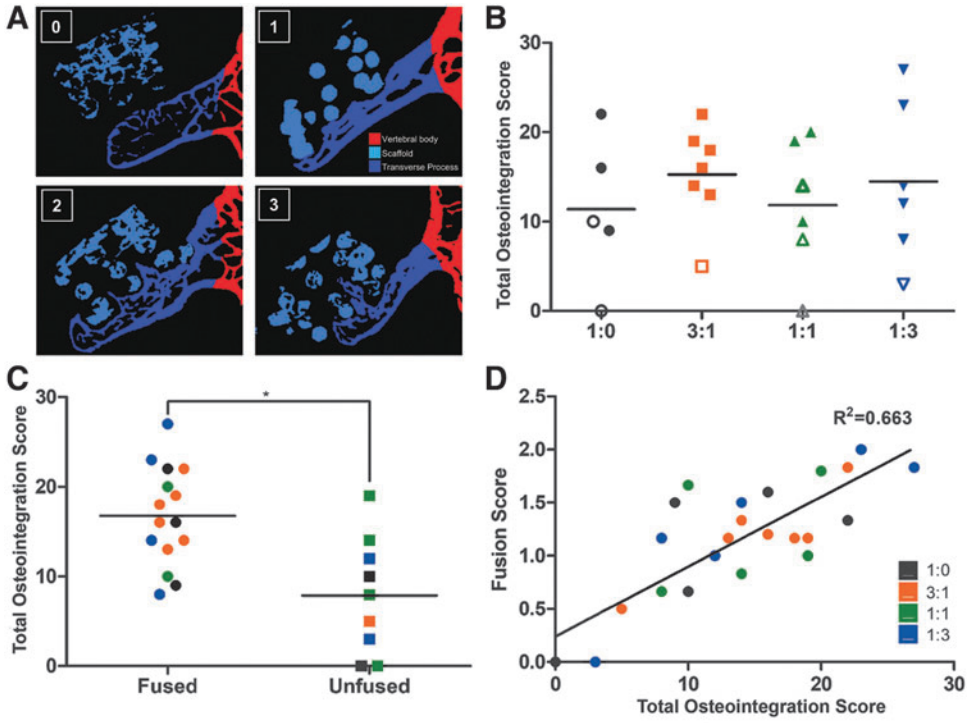

FIG. 4. Laboratory microCT quantification of osteointegration and comparison with fusion scores. **(A)** Representative segmented microCT slices illustrating the osteointegration scoring system, with the synthetic HA particles segmented *cyan*, the transverse processes and bone growing from them labeled *blue*, and all other bones shown in *red*. Each side of the spine was scored separately on a 0–3 scale (labels for each score in the *upper left* corner of each image): 0: no bone growth beyond the proximal (ventral) surface of scaffold; 1: bone growth beyond the proximal surface, but not beyond the first scaffold strut; 2: bone growth beyond the first scaffold strut, but not the second; and 3: bone growth beyond the second scaffold strut. All the slices covering a scaffold were examined, with the highest score observed assigned to that scaffold. **(B)** Total osteointegration scores. Three regions within each scaffold were scored separately for each TP: the medial end of the scaffold (the ''medial endcap,'' adjacent to the vertebral body), the scaffold body, and the lateral end of the scaffold (the ''lateral endcap''). Scores from each region were summed to generate a total ingrowth score. *Solid* and *hollow markers* denote fused and unfused spines, respectively. **(C)** Fused spines averaged a significantly greater total osteointegration score relative to unfused spines ($p < 0.01$). **(D)** Total osteointegration score versus manual palpation-based fusion score. Linear regression shows a correlation $R^2 = 0.663$, with a slope significantly different than 0 ($p < 0.001$).

adhere to and proliferate on both iterations of the scaffolds over this time frame, demonstrating that incorporation of the DBM particles into the ink does not adversely impact biocompatibility of the scaffolds (Fig. 1D).

Spine fusion

Radiographic imaging shows bilateral placement of the scaffolds at the L4–L5 TPs (Fig. 2A). As expected, scaffolds containing more HA show comparatively greater radiopacity comparatively. Because DBM is radiolucent, 0:1 HA:DBM implants were not visible by radiography. Mean fusion scores, as defined by motion or lack thereof between the L4–L5 segments, were higher among animals treated with HA-containing scaffolds (Table 2), suggesting a critical role for improved osteoconductivity in enhancement of DBM efficacy. The 0:1 HA:DBM group (which received scaffolds containing only DBM and no HA) averaged the lowest fusion score (0.78 ± 0.52; Fig. 2B), whereas the highest fusion score was found in the 3:1 HA:DBM treatment group (1.4 ± 0.37). Although all HA-containing scaffold groups resulted in fusion scores higher than the DBM-only group, the 3:1 HA:DBM treatment group was the only scaffold to significantly outperform the DBM-only treatment group (fusion rates of 92% [11/12 spines] vs. 33%, respectively; $p < 0.01$; Fig. 2C).

New bone formation and scaffold osteointegration

Figure 3A shows representative laboratory microCT images for each group. After 8 weeks implantation, disorganization of scaffold struts increased with decreasing HA content (Fig. 3A, column 1). The new bone volume was relatively small relative to that of the TP (Fig. 3A, column 2), which was presumed due to the slow degradation rate of the HA. Column 3 rows a–e, respectively, show the range of structures observed: (a) a bone ''finger'' grown from the TP deep into a macropore; (b) bone encapsulating multiple scaffold struts (arrows) and the medial endcap of the scaffold; (c) bone encapsulating a single strut (arrow); (d) a lateral endcap of the scaffold; and (e) parallel bone fingers and possible medial and lateral endcaps. DBM-only scaffolds were radiolucent and therefore not visible using laboratory microCT imaging, but some degree of bone ingrowth was still visible (row e).

Total osteointegration score did not vary statistically among groups with HA-containing scaffolds (Fig. 4B). Fused

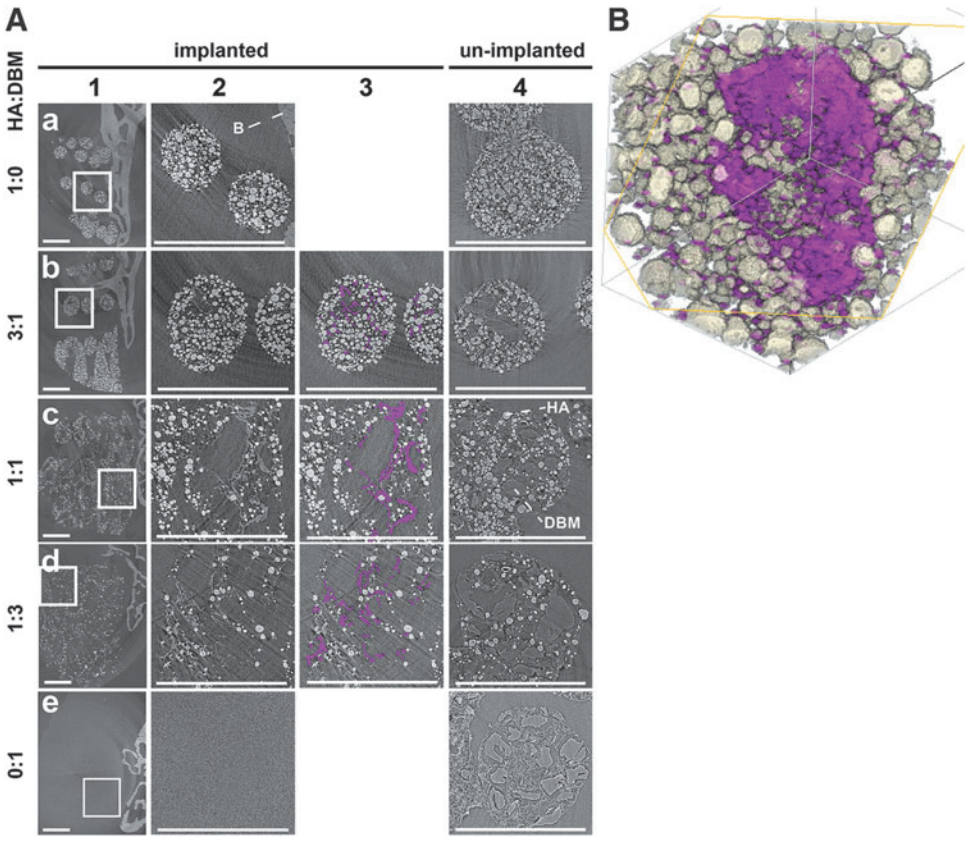

FIG. 5. Synchrotron microCT, with projections every 0.12° over 180° using 22.5 keV x-radiation and reconstructed with 2.35 μm isotropic voxels. **(A)**. *Each row* (*a–e*) depicts a different scaffold type, with HA:DBM composition on the *left*. *Column 1* shows slices of 8-week explanted scaffolds and nearby bone. Note that scaffolds containing DBM only (no HA particles) were not visible (*row e*). The area within the *solid white box* in *column 1* is enlarged in *columns 2* and *3*. *Column 3* shows the same images as *column 2*, but with bone spicules segmented in *magenta*. No bone spicules were present in either the HA-only or the DBM-only scaffolds (*rows a* and *e*, respectively). For comparison, unimplanted scaffolds were also imaged (*column 4*), and the DBM particles and the PLG elastomer are clearly visible. Note, HA and DBM particles are labeled in the 1:1 HA:DBM scaffolds only. Scale bars = 1 mm. The lighter the pixel, the more absorbing the corresponding voxel. Spicule contrast was similar to that of native bone; within one 1:3 HA:DBM slice and on an 8 bit contrast range (0 minimum to 255 maximum), two 10×10 voxel areas of spicules had mean contrast ± standard deviations of 150 ± 30 and 150 ± 25 and 10×10 areas of bone and HA had contrasts of 144 ± 16 and 204 ± 167, respectively. **(B)** A 3D rendering of a spicule within a strut of a 1:1 HA:DBM scaffold 8 weeks postoperative. The HA particles are shown in *white*, and the spicule is segmented in magenta.

spines, however, averaged a significantly higher osteointegration score than unfused spines (Fig. 4C, $p < 0.01$), and linear regression showed that osteointegration score correlated with fusion score (Fig. 4D, $R^2 = 0.633$, $p < 0.001$).

Osteointegration could not be quantified for the DBM-only scaffolds, because these scaffolds were invisible with microCT. Bone ''fingers'' were observed growing from the dorsal TP surfaces into the volume containing these DBM-only scaffolds, which was presumed as growing into the scaffold macropores. The bone ingrowth periodicity averaged 1.15 mm apart, which matched the macropore spacing in the unimplanted DBM scaffolds (1.14 mm).

Total bone volume quantified on microCT at the 8-week time point did not differ among groups (Fig. 3B). Importantly, TP bone was necessarily included in that quantification, so this result reflects the relatively small volume of new bone compared to the total bone (including TPs). Similarly, TP surface area after 8 weeks did not vary (data not shown).

Spicule formation

Figure 5 depicts representative synchrotron microCT images, with 8-week explants (columns 1–3) and unimplanted scaffolds (column 4) shown for comparison. Fine bone spicules were seen in many open volumes *within* scaffold struts, and manual segmentation shows these spicules in magenta (column 3). The spicules have contrast indistinguishable from native bone (Fig. 5), and like native bone, the volume elements (voxels) are less attenuating than those of the HA particles demonstrating that they are mineralized tissue. No spicules were observed in unimplanted scaffold material (column 4), in scaffolds without *both* HA and DBM, outside scaffold boundaries, or outside scaffold struts. DBM particles are visible in unimplanted scaffolds via X-ray phase contrast [light–dark fringes at the particle-air boundaries (column 4)], and the open volumes within implanted scaffold struts have the same shapes and ranges of sizes as the DBM particles in the unimplanted scaffolds.

Histology (Fig. 6) shows that DBM particles are still present within the scaffold struts after 8 weeks implantation, but not visualized in synchrotron microCT slices (Fig. 5).

The mineralized spicules are thin, irregularly shaped, and generally follow DBM particle surfaces. Spicules extend above and below the slice plane (columns 2 and 3), with a typical mineralized appearance (Fig. 5b).

Histology

Figure 6 shows stained thin sections of a representative spine for each group. Both DBM and PLG were still present after 8 weeks implantation. Both staining protocols show evidence of residual bone matrix at the sites of DBM particles (Fig. 6). As expected, DBM particles are visible only in the struts of DBM-containing scaffolds, with no staining within 100% HA scaffold struts. Cells were not observed near any spicules.

Discussion

Although HA and DBM enhance osteogenesis, neither alone produces high spine fusion rates clinically. In this study, we hypothesized that incorporating DBM particles into 3D printed HA scaffolds would add osteoinductivity and increase osteointegration, resulting in lack of motion between the L4–L5 segments in the established PLF rat model. We investigated different HA:DBM ratios and found that all HA:DBM composites performed well (statistically equivalent fusion scores). Of these, the 3:1 HA:DBM scaffolds had the highest mean fusion score and performed significantly better than DBM-only scaffolds. The 3:1 HA:DBM composite achieved the highest fusion rate (92% vs. 67% for the next highest group), which is remarkable because neither recombinant growth factors nor other osteoinductive pharmaceuticals were used.

With stabilization of the L4–L5 vertebral segment as a major goal, beyond manual palpation, microCT imaging was also used to quantify osteointegration, defined here by the extent to which new bone grew into and/or around the scaffold. Our data demonstrate that osteointegration was achieved in spines with high fusion scores supporting its use as a strong indicator of stability from this type of implant. We note that the total volume of new bone formed between the L4–L5 TPs was small, and we hypothesize that the stiffness of the scaffolds provided a significant degree of ''stress shielding,'' which would limit the driving force for new bone formation where it was not structurally necessary. If this were indeed the case, then the bone formation rate between the TPs might be increased by choosing a mineral phase and polymer binder that degrade more rapidly than those chosen for this study, which would provide a steadily decreasing stiffness.

A few specimens showed substantial postoperative TP scaffold separation, probably resulting from animal movement. This likely limited bone growth into those particular scaffolds and may have increased standard deviations in overall osteointegration and fusion scores. This suggests that in conditions where surgical instrumentation is used to limit migration of the scaffold, this material could prove even more successful.

In scaffold struts, spicules with the same X-ray contrast as bone were observed only within DBM particles surrounded by HA, and none grew within DBM-only or HA-only scaffolds. The spicules followed the DBM particle boundaries (e.g., Fig. 5), suggesting that DBM acts as a substrate

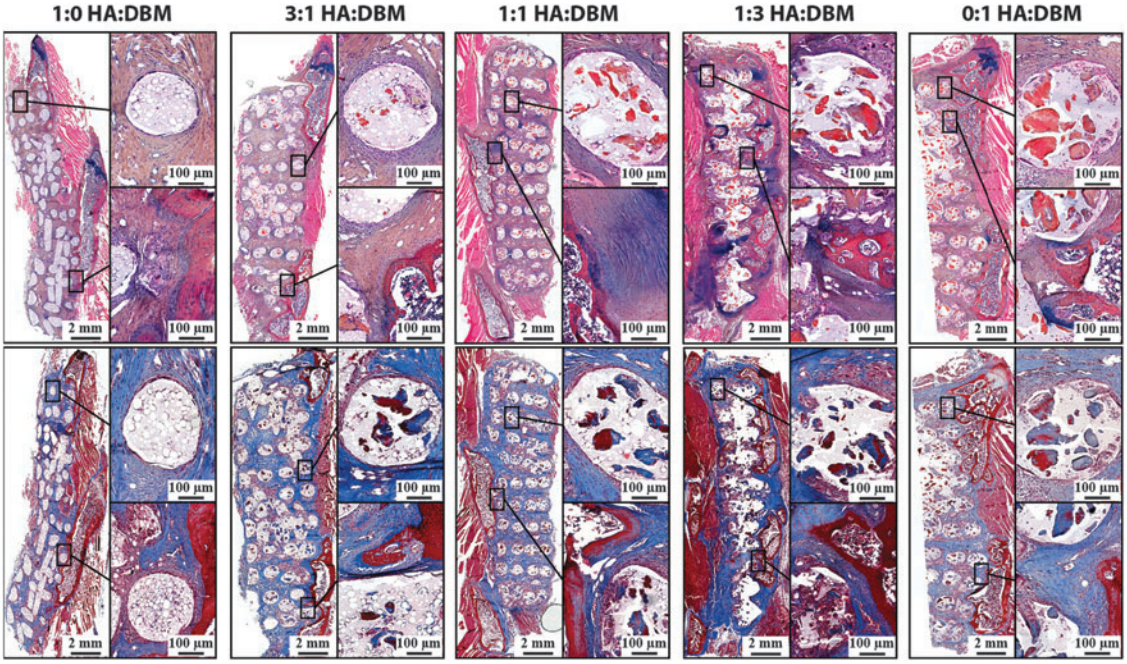

FIG. 6. Histology. Decalcified spines were sectioned to visualize the constituents of the 8-week postoperative explanted scaffolds. The *upper panel* shows sections stained with alcian blue/hematoxylin/orange-eosin Y, where cartilage stains *blue*, bone matrix *orange/red*, and soft tissue stains *pink*. The *lower panel* shows sections stained with Masson's Trichrome, where collagen stains *blue* and bone matrix stains *dark red*.

for nucleation of calcification when supraphysiological local concentrations of Ca^{2+} and PO_4^- are present. Otherwise, osteoinductivity from the osteogenic growth factors within DBM appears insufficient to induce *de novo* calcification.

Cells were not noted near any of the DBM particles (Fig. 6), suggesting that spicule formation (Fig. 5) is cell-independent. However, cells could be nearby but out of the section or could act at a distance, for example, by secreting bone sialoprotein or other HA-nucleating proteins. Whether the mineralized spicules contain HA and have a bone mesostructure (i.e., specific HA crystallography relative to collagen fibrils) remains to be determined.

Regardless of the mesostructure, these bony spicules could play an important role in the long-term fusion of vertebral segments. Once they are exposed to the matrix (i.e., through scaffold degradation) between struts, osteoclasts may be attracted to the collagen-calcified tissue structures and may initiate the bone remodeling/replacement cycle. Moreover, relative to the HA particles, the DBM particles have larger diameters. Since the mineralized spicule ''shell'' would likely prevent ion flow and mineral nucleation within a given DBM particle's central volume, the same volume fraction of smaller diameter DBM particles might greatly increase its formation.

Conclusions

The development of a recombinant growth factor-free bone graft substitute for spine fusion could eliminate risks of autograft harvest and potent exogenous growth factors. Toward this goal, we developed 3D printable scaffolds containing both osteoconductive HA and osteoinductive DBM. Our work suggests that the osteoinductive properties of the DBM could only be realized upon colocalization with Ca^{2+} and PO_4^- from the adjacent HA particles. We believe this is the first report of bone formation within a printed ceramic material's microarchitecture. This success in a preclinical PLF model (fusion rates approaching 100%) suggests promise as a nonrecombinant growth factor-based bone graft substitute. Ongoing studies are optimizing scaffold degradation rate and investigating effects of 3D printed scaffold architecture on robustness of bone formation, osteointegration, and vascular infiltration for spine fusion.

Disclosure Statement

J.A.D., R.L., K.C., M.H., G.S., A.D.S., K.M.K., C.S., C.Y., M.N., T.M., X.L., K.B., W.K.H., S.R.S., and E.L.H. have no commercial associations that might create a conflict of interest in connection with this work. A.J. and R.S. are cofounders of and shareholders in Dimension Inx, LLC, which develops and manufactures new advanced manufacturing compatible materials and devices for medical and nonmedical applications, including some of the materials developed and utilized in this work. As of August 2017, A.E.J. is currently full-time Chief Technology Officer of Dimension Inx, LLC, and R.N.S. serves part time as Chief Science Officer of Dimension Inx LLC. A.E.J. and R.N.S. are inventors on relevant patents that are licensed to Dimension Inx LLC. Dimension Inx owns the trademark for Hyperelastic Bone®. Dimension Inx LLC did not influence the conduct, description or interpretation of the findings in this report. No other authors have commercial interests in the materials described in this work.

Funding Information

This study was supported by the National Institute of Arthritis, Musculoskeletal, and Skin Diseases, grant R01AR069580. A pilot grant from the Northwestern University Clinical and Translational Sciences (NUCATS) program also supported part of this work. We thank Danielle Chun, Joseph Weiner, Michael Schallmo, Ralph Cook, and John Yun for contributing as surgeons. This research used resources of the APS, a U.S. DOE Office of Science User Facility operated by Argonne National Laboratory under Contract No. DE-AC02-06CH11357; Northwestern's EPIC facility, NU*ANCE* Center supported by the Soft and Hybrid Nanotechnology Experimental Resource (NSF ECCS-1542205), the MRSEC program (NSF DMR-1720139) at the Materials Research Center, the International Institute for Nanotechnology (IIN), the Keck Foundation and the State of Illinois, through the IIN; Northwestern's Center for Advanced Microscopy (National Cancer Institute Cancer Center Support Grant P30 CA060553 to the Robert H. Lurie Comprehensive Cancer Center); and Northwestern's Histology and Phenotyping Laboratory (Robert H. Lurie Comprehensive Cancer Center support grant NCI CA060553). A.J. was partially supported through a postdoctoral fellowship by The Hartwell Foundation.

References

1. Rajaee, S.S., Bae, H.W., Kanim, L.E., and Delamarter, R.B. Spinal fusion in the United States: analysis of trends from 1998 to 2008. Spine **37,** 67, 2012.
2. Dimar, J.R., II, Glassman, S.D., Burkus, J.K., Pryor, P.W., Hardacker, J.W., and Carreon, L.Y. Two-year fusion and clinical outcomes in 224 patients treated with a single-level instrumented posterolateral fusion with iliac crest bone graft. Spine J **9,** 880, 2009.
3. Ondra, S.L., and Marzouk, S. Revision strategies for lumbar pseudarthrosis. Neurosurg Focus **15,** E9, 2003.
4. Raizman, N.M., O'Brien, J.R., Poehling-Monaghan, K.L., and Yu, W.D. Pseudarthrosis of the spine. J Am Acad Orthop Surg **17,** 494, 2009.
5. Nickoli, M.S., and Hsu, W.K. Ceramic-based bone grafts as a bone grafts extender for lumbar spine arthrodesis: a systematic review. Global Spine J **4,** 211, 2014.
6. Kaiser, M.G., Groff, M.W., Watters, W.C., III, et al. Guideline update for the performance of fusion procedures for degenerative disease of the lumbar spine. Part 16: bone graft extenders and substitutes as an adjunct for lumbar fusion. J Neurosurg Spine **21,** 106, 2014.
7. Urist, M.R. Bone: formation by autoinduction. Science **150,** 893, 1965.
8. Urist, M.R. Bone Transplants and Implants. Fundamental and Clinical Bone PHysiology. Philadelphia: JB Lippincott, 1980. p. 331.
9. Urist, M.R., and Dawson, E. Intertransverse process fusion with the aid of chemosterilized autolyzed antigen-extracted allogeneic (AAA) bone. Clin Orthop 97, 1981.
10. Fu, R., Selph, S., McDonagh, M., et al. Effectiveness and harms of recombinant human bone morphogenetic protein-2 in spine fusion: a systematic review and meta-analysis. Ann Intern Med **158,** 890, 2013.
11. Epstein, N.E. Basic science and spine literature document bone morphogenetic protein increases cancer risk. Surg Neurol Int **5,** S552, 2014.
12. Carragee, E.J., Hurwitz, E.L., and Weiner, B.K. A critical review of recombinant human bone morphogenetic protein-

2 trials in spinal surgery: emerging safety concerns and lessons learned. Spine J **11,** 471, 2011.
13. Jakus, A.E., Rutz, A.L., Jordan, S.W., et al. Hyperelastic ''bone'': a highly versatile, growth factor-free, osteoregenerative, scalable, and surgically friendly biomaterial. Sci Transl Med **8,** 358ra127, 2016.
14. Alluri, R., Jakus, A., Bougioukli, S., et al. 3D printed hyperelastic ''bone'' scaffolds and regional gene therapy: a novel approach to bone healing. J Biomed Mater Res A **106,** 1104, 2018.
15. Jakus, A.E., Geisendorfer, N.R., Lewis, P.L., and Shah, R.N. 3D-printing porosity: a new approach to creating elevated porosity materials and structures. Acta Biomater **72,** 94, 2018.
16. Hsu, W.K. Outcomes following nonoperative and operative treatment for cervical disc herniations in National Football League athletes. Spine **36,** 800, 2011.
17. Hsu, W.K., Wang, J.C., Liu, N.Q., et al. Stem cells from human fat as cellular delivery vehicles in an athymic rat posterolateral spine fusion model. J Bone Joint Surg Am **90,** 1043, 2008.
18. Lee, S.S., Hsu, E.L., Mendoza, M., et al. Gel scaffolds of BMP-2-binding peptide amphiphile nanofibers for spinal arthrodesis. Adv Healthc Mater **4,** 131, 2015.
19. Hsu, E.L., Sonn, K., Kannan, A., et al. Dioxin exposure impairs BMP-2-mediated spinal fusion in a rat arthrodesis model. J Bone Joint Surg Am **97,** 1003, 2015.
20. Boden, S.D., Titus, L., Hair, G., et al. Lumbar spine fusion by local gene therapy with a cDNA encoding a novel osteoinductive protein (LMP-1). Spine (Phila Pa 1976) **23,** 2486, 1998.
21. Abe, Y., Takahata, M., Ito, M., Irie, K., Abumi, K., and Minami, A. Enhancement of graft bone healing by intermittent administration of human parathyroid hormone (1-34) in a rat spinal arthrodesis model. Bone **41,** 775, 2007.
22. van Gaalen, S.M., Dhert, W.J., van den Muysenberg, A., et al. Bone tissue engineering for spine fusion: an experimental study on ectopic and orthotopic implants in rats. Tissue Eng **10,** 231, 2004.
23. Bright, C., Park, Y.S., Sieber, A.N., Kostuik, J.P., and Leong, K.W. In vivo evaluation of plasmid DNA encoding OP-1 protein for spine fusion. Spine (Phila Pa 1976) **31,** 2163, 2006.
24. Miyazaki, M., Sugiyama, O., Zou, J., et al. Comparison of lentiviral and adenoviral gene therapy for spinal fusion in rats. Spine (Phila Pa 1976) **33,** 1410, 2008.
25. Cui, Q., Ming Xiao, Z., Balian, G., and Wang, G.J. Comparison of lumbar spine fusion using mixed and cloned marrow cells. Spine (Phila Pa 1976) **26,** 2305, 2001.
26. Glaeser, J.D., Salehi, K., Kanim, L.E.A., et al. Anti-inflammatory peptide attenuates edema and promotes BMP-2-induced bone formation in spine fusion. Tissue Eng Part A **24,** 1641, 2018.

Address correspondence to:
Erin L. Hsu, PhD
Department of Orthopaedic Surgery
Northwestern University
Lurie Medical Research Building
303 E. Superior Street, 11-107
Chicago, IL 60611

E-mail: e-hsu@northwestern.edu

Received: June 24, 2019
Accepted: August 23, 2019
Online Publication Date: September 26, 2019